

PCCP

Physical Chemistry Chemical Physics

Accepted Manuscript

This article can be cited before page numbers have been issued, to do this please use: J. Sun, X. Zhong, W. Cui, J. Shi, J. Hao, M. Xu and Y. Li, *Phys. Chem. Chem. Phys.*, 2020, DOI: 10.1039/C9CP05084A.



This is an Accepted Manuscript, which has been through the Royal Society of Chemistry peer review process and has been accepted for publication.

Accepted Manuscripts are published online shortly after acceptance, before technical editing, formatting and proof reading. Using this free service, authors can make their results available to the community, in citable form, before we publish the edited article. We will replace this Accepted Manuscript with the edited and formatted Advance Article as soon as it is available.

You can find more information about Accepted Manuscripts in the [Information for Authors](#).

Please note that technical editing may introduce minor changes to the text and/or graphics, which may alter content. The journal's standard [Terms & Conditions](#) and the [Ethical guidelines](#) still apply. In no event shall the Royal Society of Chemistry be held responsible for any errors or omissions in this Accepted Manuscript or any consequences arising from the use of any information it contains.

The intrinsic magnetism, quantum anomalous Hall effect and Curie temperature in 2D transition metal trihalides

Jiaxiang Sun^{⊥,1}, Xin Zhong^{⊥,2}, Wenwen Cui³, Jingming Shi³, Jian Hao^{*,3}, Meiling Xu^{*,3} and Yinwei Li³

¹Department of Informationization Construction and Management, Information and Network Center, Jiangsu Normal University, Xuzhou 221116, China

²Center for High Pressure Science and Technology Advanced Research, Changchun 130012, China

³School of Physics and Electronic Engineering, Jiangsu Normal University, Xuzhou 221116, China

Corresponding Authors:

jian_hao@jsnu.edu.cn, xuml@jsnu.edu.cn

Abstract

Searching for experimentally feasible intrinsic quantum anomalous Hall (QAH) insulators is of great significance for dissipationless electronics applications. Here we predict, based on density functional theory (DFT), that four monolayer transition metal tri-bromides (VBr₃, FeBr₃, NiBr₃, and PdBr₃) are endowed with intrinsic half-metallicity and possess quantum anomalous Hall insulating phases. DFT+U calculations reveal that VBr₃, NiBr₃, and PdBr₃ monolayers undergo nontrivial to Mott insulators transition with increasing on-site Hubbard Coulomb interaction U at 0.5, 2 and 3 eV. The gap opening induced by the spin-orbit coupling drives the systems into the QAH state. The Curie temperatures of VBr₃, NiBr₃, and PdBr₃ monolayers are ~190, 100 and 110 K. Additionally, the calculated cleavage energies suggest that the freestanding VBr₃, FeBr₃, NiBr₃, and PdBr₃ monolayers can be easily produced from exfoliation using adhesive tape, which may stimulate experimental research interest to achieve QAH phases.

Introduction

The quantum anomalous Hall (QAH) effect, arising from time-reversal symmetry broken via internal magnetization, was first proposed by Haldane in a 2D honeycomb lattice.¹ Unfortunately, not much progress towards the realization of the QAH effect has been made because the host material of the 2D honeycomb-lattice was believed to be unrealistic up until graphene was successfully exfoliated in 2004.² The experimental realization of graphene not only raised the hope of achieving QAH effect in a real 2D honeycomb-lattice system^{3–5}, but also made the era of 2D materials come^{6–8}.

Recently, this long-sought QAH effect has been predicted in graphene by adsorbing transition metal atoms or proximity coupling to an ferromagnetic (FM) or anti ferromagnetic (AFM) insulator,^{9–13} and experimentally observed in V- or Cr-doped (Bi, Sb)₂Te₃ topological insulator.^{14–17} Realization of QAH phases is of great significance both in fundamental physics and in dissipationless electronics applications.^{18,19}

Despite the numerous theoretical predictions and experimental researches, there are limitations for the current study of real QAH materials. The QAH phase in graphene decorated with heavy adatoms has not been realized thus far.^{20,21} Actually, introducing a long-range FM order by doping in insulating films is quite tough task in carrying out experiments with the QAH effect²². In addition, the synthesis of such thin film basing on molecular beam epitaxy is expensive and difficult to manipulate. Thus, recent efforts^{23–27} have focused on searching for experimentally feasible intrinsic QAH insulators.

Very recent experimental discovery of intrinsic two dimensional (2D) ferromagnetic semiconductors^{28,29} have received much attention not only of experimentally feasibility²⁸ but also of internal ferromagnetism^{25,26,30–33} which might

achieve highly desirable QAH effect. It has been theoretically predicted that several 2D transition-metal tri-halides can host the QAH effect, such as RuI_3 ³⁴, ReX_3 ³⁵ ($\text{X}=\text{Br}, \text{I}$), and MnX_3 ³⁶ ($\text{X}=\text{F}, \text{Cl}, \text{Br}, \text{I}$). And more importantly, the 3D layered crystals with the weak interlayer van der Waals interactions are easily exfoliated down to 2D monolayers.^{37–39}

Here we studied 14 transition metal tri-bromides monolayers based on the first principles calculations, and found that VBr_3 , FeBr_3 , NiBr_3 , and PdBr_3 are endowed with intrinsic half-metallicity and possess the quantum anomalous Hall insulating phases. The nontrivial states emerge of VBr_3 , NiBr_3 , and PdBr_3 at the Fermi level when the $U < 0.5, 2$, and 3 eV. Upon further increasing the effective on-site Hubbard Coulomb interaction, it undergoes a transition from the nontrivial to the Mott insulating state. The topological nontrivial properties of monolayer VBr_3 were identified by calculations of the Berry curvature and the corresponding edge states. Besides, the Curie temperature is $\sim 190, 100$ and 110 K for VBr_3 , NiBr_3 and PdBr_3 and the Néel temperature of FeBr_3 is calculated to be 70 K.

Computational methods

Our first-principles calculations are based on the density functional theory (DFT)⁴⁰ as implemented in the Vienna ab initio simulations package (VASP)⁴¹. The external potential is given by the projector augmented-wave (PAW) approximation⁴², and the exchange-correlation functional is given by the generalized gradient approximation parameterized by Perdew, Burke, and Ernzerhof (GGA-PBE)⁴³. The electron-ion interaction was described by the projector augmented-wave potentials, with $4p^63d^44s^1$ and $4s^24p^5$ configurations treated as the valence electrons of V and Br, respectively. The plane-wave cutoff energy is set to be 500 eV in all first-principles calculations, and the

first Brillouin zone is sampled using a Γ -centered $(11 \times 11 \times 1)$ Monkhorst-Pack grid⁴⁴. The convergence criteria for energy and the ionic force were set 10^{-5} eV and 0.01 eV/Å, respectively. Sufficient vacuum was used along z direction i.e. perpendicular to the 2D sheet, to avoid spurious interaction among the periodic images. The SOC was included in the self-consistent calculations. The effective Hubbard U term is considered to address the self-interaction error of the generalized gradient approximation⁴⁵. The dynamic stability of monolayer VBr_3 was verified by phonon dispersion analyses through the direct supercell method, as implemented in the PHONOPY code. Ab initio molecular dynamic (AIMD) simulations were performed with the Nosé-Hoover thermostat to confirm the thermal stability. Based on the Wannier functions⁴⁶ obtained from the first-principles calculations, we constructed the edge Green's function of the semi-infinite VBr_3 monolayer. The Berry curvature were calculated by the Wannier interpolation. In order to integrate Berry curvature, a much denser k mesh of $(120 \times 120 \times 1)$ was adopted.

Results and discussions

A. Structure and electronic structures of monolayer transition metal tri-bromides

Reality, transition metal tri-halides MX_3 (M is a metal cation and X is a halogen anion) have been reported to adopt either the monoclinic $AlCl_3$ structure type or the rhombohedral BiI_3 structure type⁴⁷, as illustrated in Fig. 1. The monolayer structure of transition metal tri-bromides is composed of a honeycomb net of M metal cations that are in edge sharing octahedral coordination, derived from bulk. In octahedral coordination environments of the M atoms, electronic and magnetic properties can be tuned by its electron configuration. The electronic structures of transition metal tri-bromides we considered in this study using the PBE functional are shown in Fig. S1 and

S2. We can find that (1) most of transition metal tri-bromides are ferromagnetic except nonmagnetic CoBr_3 and RhBr_3 ; (2) most of the ferromagnetic materials are half-metallic except semiconductors CrBr_3 and MoBr_3 ; (3) most of the half-metallic materials can host Dirac point except ZrBr_3 ; (4) the spin-polarized massless Dirac fermions of VBr_3 , FeBr_3 , NiBr_3 and PdBr_3 are found at the high-symmetry K point of the Brillouin zone. Then, we focus on further analyze the structure characters, electronic and magnetic properties of VBr_3 , FeBr_3 , NiBr_3 and PdBr_3 .

B. Structure and stability

The optimized structures of MBr_3 ($\text{M}=\text{V}$, Fe , Ni , and Pd) monolayers are composed of a Br-M-Br sandwich where a sheet of M atoms are sandwiched between two sheets of Br atoms. The unit cell is composed of two M atoms and six Br atoms, and the M is the octahedral coordination with Br atoms. The corresponding lattice constants and bond lengths of VBr_3 , FeBr_3 , NiBr_3 and PdBr_3 are listed in Table 1. We have studied the lattice dynamics adopted (3×3) supercells by calculating the phonon dispersions. As presented in Fig. 1c, the absence of imaginary modes in the entire Brillouin zone confirms that monolayer VBr_3 is dynamically stable. Note that FeBr_3 , NiBr_3 , and PdBr_3 monolayers are also dynamically stable^{48–50}. After heating at room temperature (300 K) with a time step of 1 fs, no structure reconstruction is found to occur, indicating they are also thermodynamically stable. The snapshots of atomic configurations of VBr_3 , FeBr_3 , NiBr_3 , and PdBr_3 monolayers at the end of AIMD simulations are shown in Fig. S3. Moreover, we have performed a first-principles swarm structural search^{51,52} and found that the structure in Fig. 1(b) is the global minimum.

C. Experimental feasibility

The weak van der Waals interaction in the layered bulk crystals allows monolayer transition metal tri-bromides to be obtained from the crystal using mechanical

exfoliation. To obtain a free-standing membrane, the cleavage energy needed to be overcome in the exfoliation process should be small. A large gap d between two layers representing a fracture in the bulk is introduced to simulate the exfoliation procedure. The cleavage energies as the function of d calculated using the optB86b-vdW functional are shown in Fig. 2. It can be seen that the cleavage energies for VBr₃, FeBr₃, NiBr₃, and PdBr₃ materials are 0.28, 0.12, 0.14, and 0.17 J m⁻² significantly smaller than that of MoS₂ (0.27 J m⁻²) and graphite (0.37 J m⁻²)⁵³. Thus, freestanding VBr₃, FeBr₃, NiBr₃, and PdBr₃ monolayers can be easily produced from exfoliation using adhesive tape.

D. Electronic properties and Curie temperature

The values of the M-Br-M angles for VBr₃, FeBr₃, NiBr₃, and PdBr₃ are 97.42°, 95.89°, 95.90° and 97.00°. According to the Goodenough-Kanamori-Anderson (GKA) rules the superexchange interaction of a 90° cation-anion-cation angle favors FM ordering whereas a 180° angle favors antiferromagnetic^{54–56}. Thus, the superexchange interactions between two nearest-neighbor M atoms mediated by Br are expected to be dominant leading to FM ground state. We consider four possible magnetic configurations (one FM and three AFM) to determine the optimal magnetic coupling, as shown in Fig. S4 and calculate the energy difference between ferromagnetic and antiferromagnetic states listed in Table S1. The FM states in VBr₃, NiBr₃ and PdBr₃ have the lowest total energy and AFM state in FeBr₃ has the lowest total energy. One of the important properties of ferromagnets and antiferromagnets is the Curie temperature and Néel temperature. Using Monte Carlo (MC) simulations based on the 2D Ising model, we have calculated the Curie temperature of VBr₃, NiBr₃ and PdBr₃ and the Néel temperature of FeBr₃. For simplicity, only the nearest neighbor (NN) exchange interaction is considered since the second and third NN exchange interactions are

smaller than the first NN interaction exchange interactions³⁶. The NN exchange-coupling parameters J can be extracted by mapping the total energies of the systems with different magnetic structures to the Ising model:

$$H = - \sum_{ij} J S_i \cdot S_j$$

where S is the net magnetic moment at the V site, i and j represent the nearest V atoms. By comparing the total energies of ferromagnetic and antiferromagnetic states (E_{ex}), the exchange parameter can be evaluated by $J = E_{\text{ex}}/6S^2$, we obtain $J = 9.2, 19$ and 20 meV for VBr_3 , NiBr_3 and PdBr_3 . For FeBr_3 , the exchange parameter is -13 meV. The positive/negative value represents FM/AFM coupling. The calculated Curie temperature is $\sim 190, 100$ and 110 K (Fig. 3) for VBr_3 , NiBr_3 and PdBr_3 , which is comparable with that of other 2D FM materials^{35,57,58}. The Néel temperature is calculated to be 70 K.

It is widely accepted that the magnetocrystalline anisotropic energy (MAE) closely correlates with the thermal stability of magnetic data storage of magnetic material. In general, the larger the MAE, the better is the performance for data storage. Here, two magnetization directions in plane, that is $[110]$ and $[1-10]$ directions, and one direction out of plane, that is, $[001]$ directions is considered, as summarized in Table S2. Among them, the in-of-plane of $[110]$, $[1-10]$, and $[110]$ directions for VBr_3 , NiBr_3 and PdBr_3 are the easy axis, respectively.

The band structure of FM ground state for VBr_3 monolayer is shown in Fig. 4 (a). The VBr_3 can be approximately characterized as a “zero-gap half-metal” in the case without spin-orbit coupling (SOC). It is almost zero gapped because of the band-toughing at the high-symmetry K point just upper the Fermi level in spin-up channel. It is nearly half-metal because of the presence of a band gap of 2.85 eV in spin-down channel. The Dirac states of VBr_3 are mainly derived from the V- d orbitals. The SOC

opens band gap of 20 meV for VBr₃ (Fig. 4a). Because the GGA usually underestimates the band gaps, the HSE06 hybrid functional is also used to check the band gaps. Our calculations show that the band gaps are 48 meV with HSE06 for VBr₃ monolayers, as seen in Fig. 4b. As shown in Fig. S1, FeBr₃, NiBr₃ and PdBr₃ monolayers are also almost zero gapped because of the band-toughing at the high-symmetry K point. However, they are semiconducting taking the HSE functional into consideration [Fig. S5].

The projected density of states (PDOS) and the projected band structures were calculated for the VBr₃ monolayer at PBE level to gain insight into the origin of electronic and magnetic properties (Fig. 5). Under the distorted octahedral crystal field of Br atoms, the *d* orbital of V would be split into one-fold *a₁* orbital corresponding to *d_{z²}* orbital and two-fold *e₁* and *e₂* orbitals corresponding to (*d_{xz}*, *d_{yz}*) and (*d_{x² - y²}*, *d_{xy}*) orbitals. The two *d* electrons with spin-up lead to partially filled *d* orbitals, giving rise to the metal character and exhibiting a high-spin $a^{\uparrow}_2 e^{\uparrow}_2 e^{\uparrow}_1 a^{\uparrow}_2 e^{\uparrow}_2 e^{\uparrow}_1$ electronic configuration. Based on Griffith's crystal field theory, the spin states of transition metal ions can be determined by the relative strength between crystal field splitting (ΔE_{cf}) and Hund exchange splitting (ΔE_{ex}) of *d* orbitals. The exchange splitting (0.96 eV) and the crystal field splitting (0.89 eV) for the VBr₃ monolayer lead to a high spin (2 μB) state which is in good agreement with the V ($a^{\uparrow}_2 e^{\uparrow}_2 e^{\uparrow}_1 a^{\uparrow}_2 e^{\uparrow}_2 e^{\uparrow}_1$) spin configuration. The calculated magnetic moment of the V atom is 1.97 $\mu\text{B}/\text{atom}$, which is consistent with the 2 $\mu\text{B}/\text{atom}$ staying in the high-spin state. Because of the hybridization with V-3*d* states, the Br-4*p* are slightly spin polarized but with an opposite moment (about -0.05 $\mu\text{B}/\text{atom}$). Allowing for the delocalized feature of the Br 4*p* states, the FM structure between the V spins is expected to emerge in a long range.

The states near the Fermi level have main contributions from the a_1 and e_2 states, while the e_1 state does not contribute significantly as shown in Fig. 5a. The whole occupied a_1 and partially occupied e_2 orbitals around the Fermi level form a Dirac point in the VBr_3 monolayer. The zero gap behavior in the up spin channel is the most important character here, because it suggests the inverted band structure around the high symmetry K point. V ion has a strong ferromagnetic ground states, leading to strong Zeeman splitting for energy states near Fermi level. The presence of exchange splitting generates that the band inversion of spin-up states occurs while the spin-down energy states maintain the normal band structure. In down spin channel, the a_1 orbit level is higher than e_2 orbit level. In a sharp contrast, the band inversion occurs between the a_1 state and e_2 orbit level in up spin channel, as evidenced by the projected band structures in Fig. 5(b).

Next, we employ DFT+U calculations to show the effect of the on-site Coulomb repulsion U on the electronic structures of VBr_3 , $FeBr_3$, $NiBr_3$ and $PdBr_3$ since d electrons of transition metal exhibit correlation effects, as shown in Fig. S6-9. We can find that U term greatly impacts the band structure of $FeBr_3$ and as the on-site Coulomb repulsion U gradually increases, the Mott insulating phases occur at U equal to 0.5, 2 and 3 eV in VBr_3 , $NiBr_3$, and $PdBr_3$ monolayers.

E. Quantum anomalous Hall effect

The existence of topologically protected chiral edge states is one of the most important consequences of the QAH state. To further reveal the nontrivial topological nature of the VBr_3 monolayer, we calculate the edge states of the VBr_3 monolayer using Green's functions based on Wannier functions obtained from PBE calculations, which reduces the cost of calculations while it does not change the topology of the electronic

structure. As shown in Fig. 6, the nontrivial edge states connecting the valence and conduction bands cross the insulating gap of the Dirac cone, confirming the nontrivial topological nature of the VBr_3 monolayer. The Berry curvature along the high-symmetry direction ($\Gamma \rightarrow \text{K} \rightarrow \text{M} \rightarrow \Gamma$) has a sharp spike of the same sign located at the K and points as shown in Fig. 6d. By integrating the Berry curvature in the entire Brillouin zone, the calculated Chern number C is -1 with a non-trivial topological state. As expected from the non-zero Chern number, the anomalous Hall conductivity shows a quantized charge Hall plateau of $\delta_{xy} = e^2 / h$ when the Fermi level is located in the insulating gap of the spin-up Dirac cone. The nontrivial topological properties of the FeBr_3 , NiBr_3 and PdBr_3 monolayers have been verified^{32,49,50}.

Conclusions

Using DFT and DFT+U calculations, we have made a systematic investigation of the electronic and magnetic structures in monolayer transition metal tri-bromides, especially that of VBr_3 , FeBr_3 , NiBr_3 and PdBr_3 monolayers. Their Dirac spin-gapless half-metallic features characterized by a band structure with an unusually large gap in one spin channel and a Dirac cone in the other spin channel at PBE level. Upon increasing the on-site Coulomb repulsion, VBr_3 , NiBr_3 and PdBr_3 monolayer undergo a quantum phase transition from QAH insulator to Mott insulator. The calculated cleavage energies suggest that the freestanding VBr_3 , FeBr_3 , NiBr_3 and PdBr_3 monolayers can be easily obtained. Additionally, the Curie temperature is ~ 190 , 100 and 110 K for VBr_3 , NiBr_3 and PdBr_3 . The Néel temperature of FeBr_3 is calculated to be 70 K. The combination of these unique properties renders monolayer transition metal tri-bromides a promising platform for potential applications in future spintronics.

[‡]J. S and X. Z. contributed equally to this work.

To whom all correspondence should be addressed.

xuml@jsnu.edu.cn; jian_hao@jsnu.edu.cn

Notes

The authors declare no competing financial interest.

ACKNOWLEDGEMENTS

The authors acknowledge funding from the National Natural Science Foundation of China under Grant Nos. 11722433, 11804128, 11804129 and 11904142. All the calculations were performed using the High Performance Computing Center of the School of Physics and Electronic Engineering of Jiangsu Normal University.

Table I. The optimized lattice constants (α , Å) and bond lengths (d , Å), and thickness (h , Å) of VBr₃, FeBr₃, NiBr₃ and PdBr₃ at PBE level. The “thickness” of this monolayer, defined as the distance between the vertical coordinates of the top-Br layer and the bottom-Br layer.

Compounds	α	d_{Br-M}	h
VBr ₃	6.61	2.54	2.92
FeBr ₃	6.36	2.45	2.80
NiBr ₃	6.30	2.45	2.81
PdBr ₃	6.67	2.57	2.87

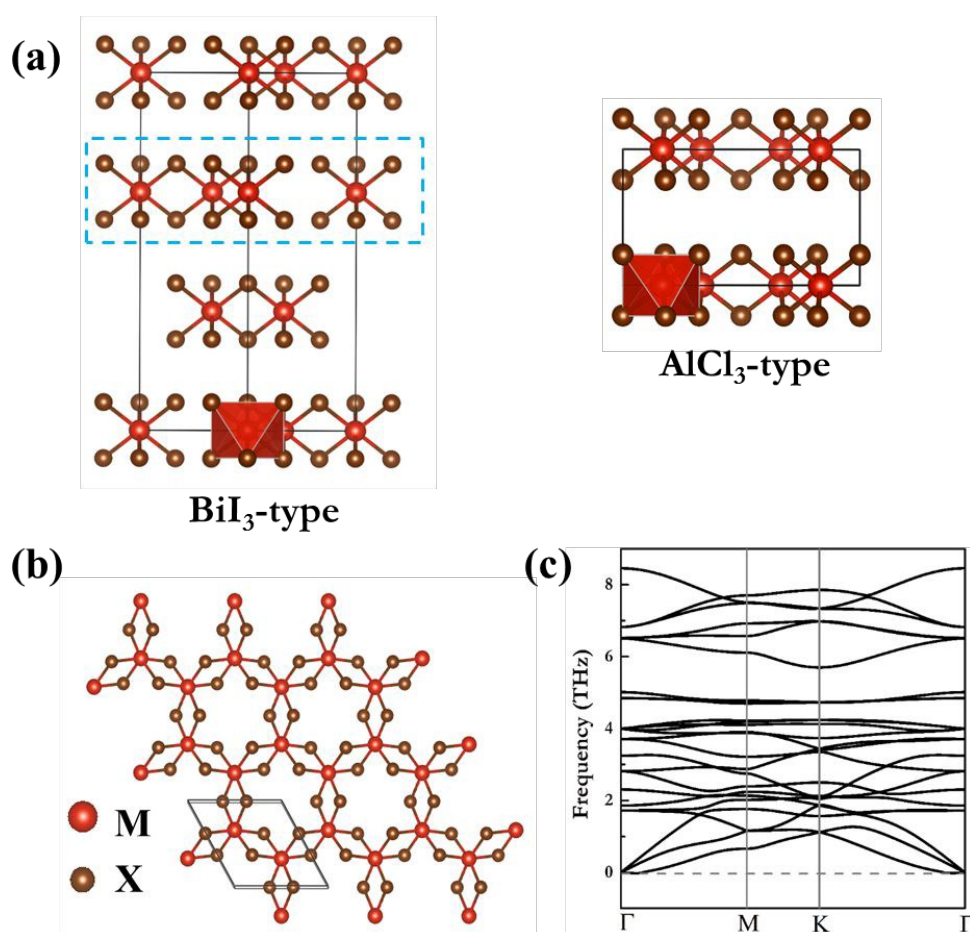


Figure 1. A side view of (a) the BiI₃ and AlCl₃ structure types and (b) a plan view of common monolayer with coordinate systems corresponding to each structure type. (c) The phonon band structure of monolayer VBr₃.

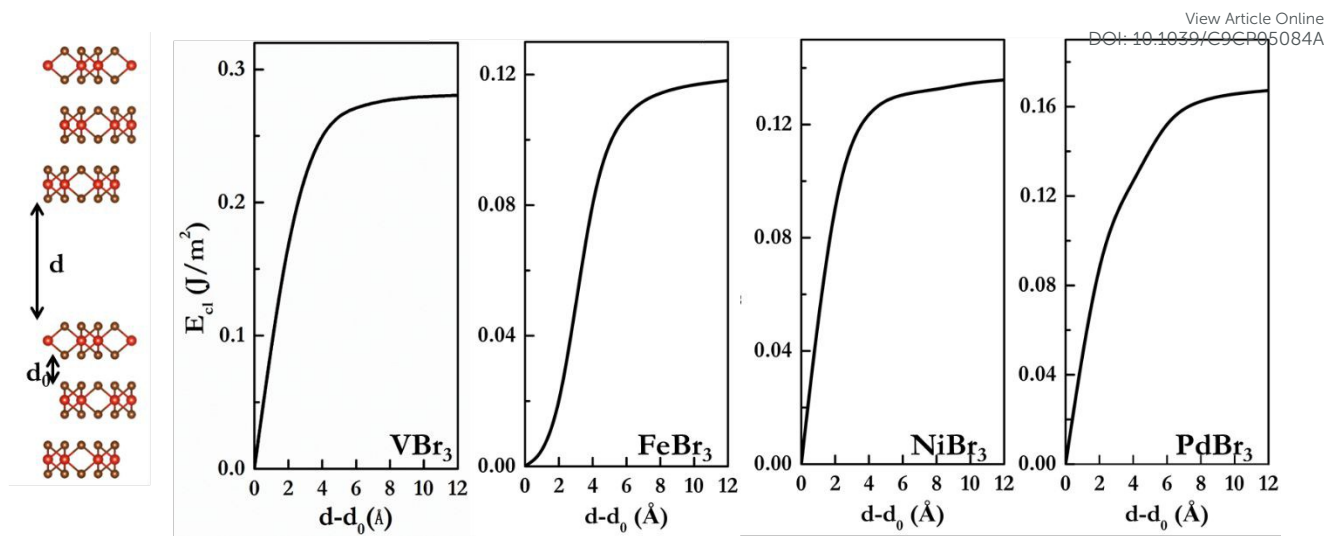


Figure 2. Supercell model used to simulate the exfoliation procedure and the cleavage energy calculated using the optB88-vdW functional as a function of the separation d between two fractured parts. d_0 represents the equilibrium interlayer distance.

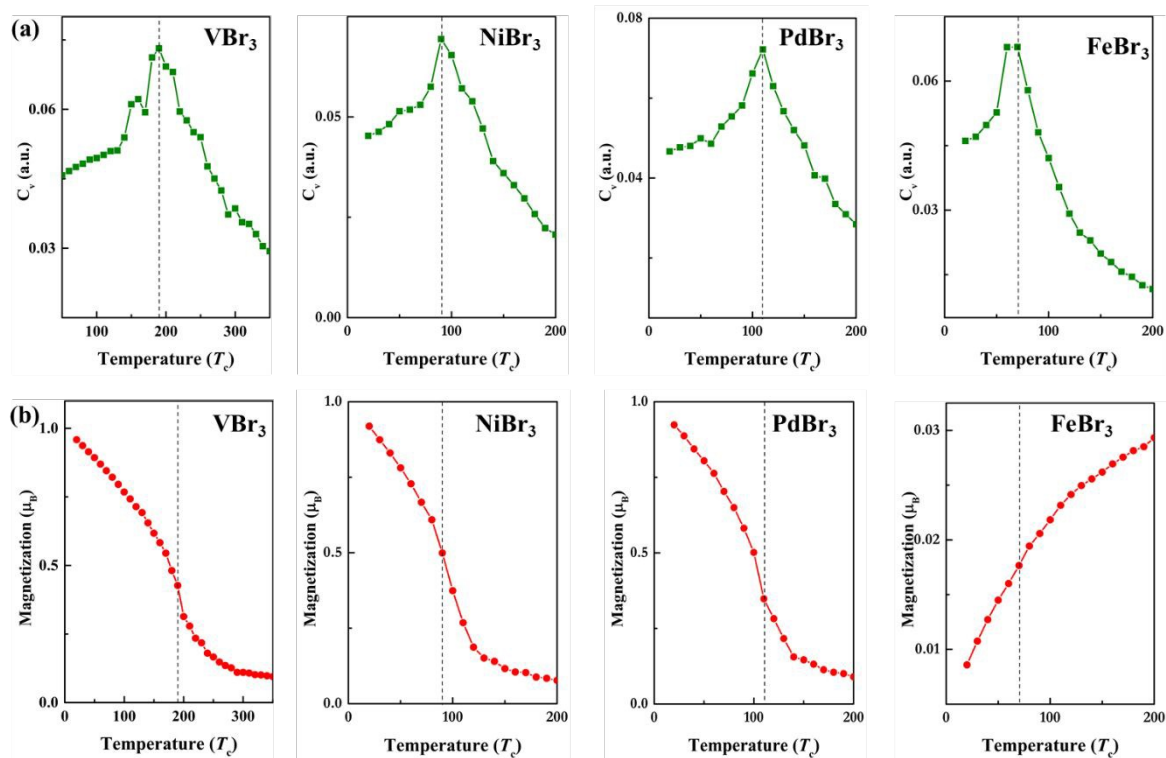


Figure 3. Temperature variation of the heat capacity (a) and the magnetic moment (b) for the VBr₃, NiBr₃, PdBr₃ and FeBr₃ monolayers.

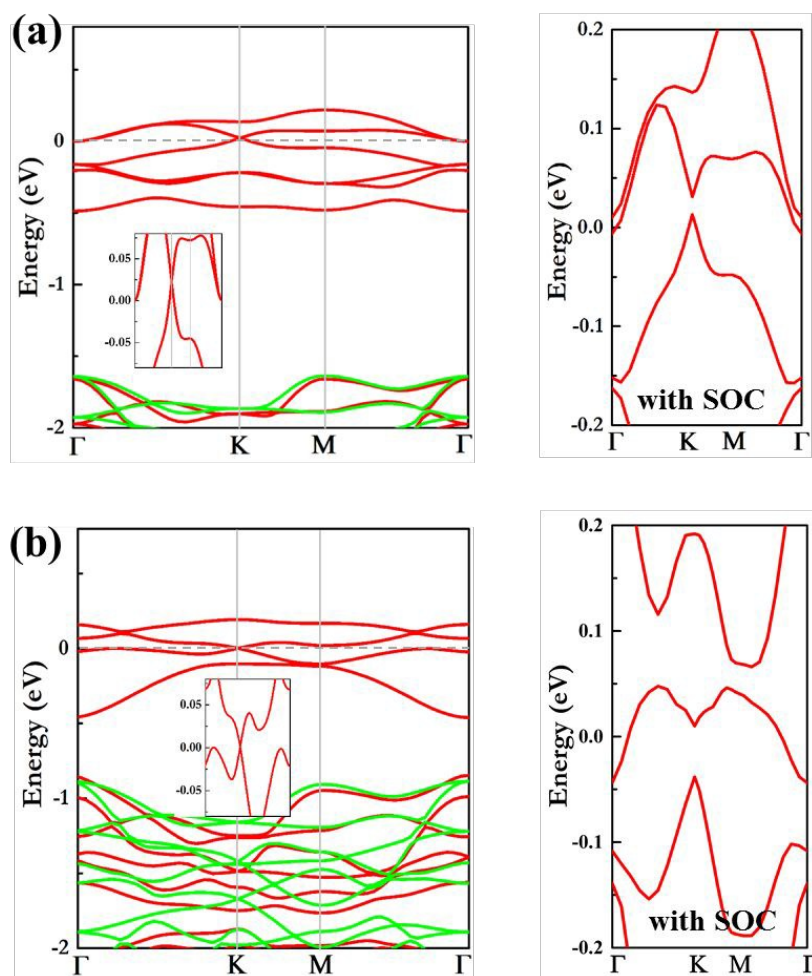


Figure 4. Spin-polarized band structures of monolayer VBr_3 without and with SOC at (a) PBE and (b) HSE06 level. Inset: Dirac states near the Fermi level. The red and green lines represent the spin up and spin down channels, respectively.

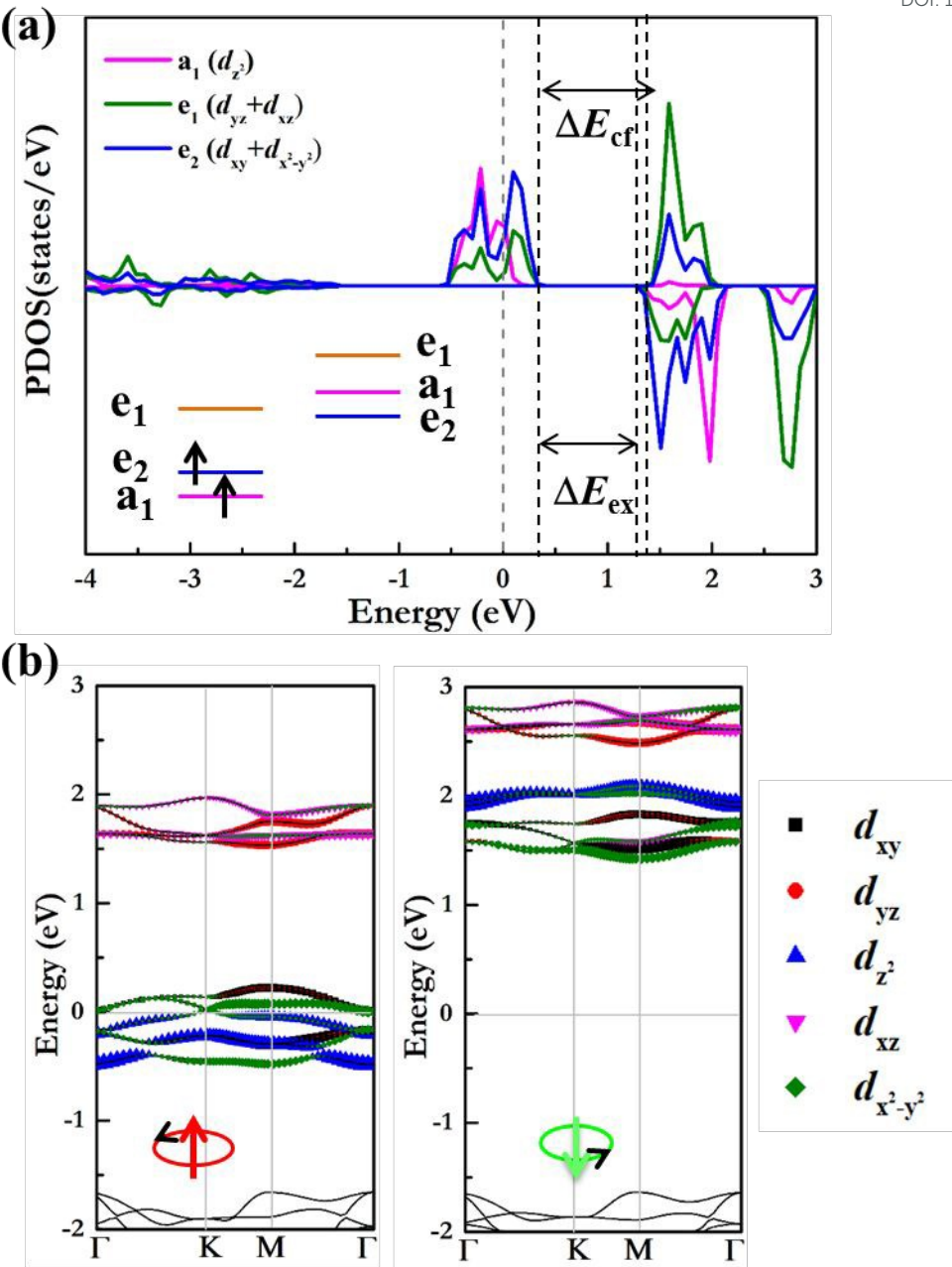


Figure 5. (a) The PDOS of d states for V atoms is shown. (b) The projected band structures without SOC (showing the up and down spin parts separately). The relative size of each symbol indicates the V atoms projection of the eigenvalue. The Fermi level is set to zero.

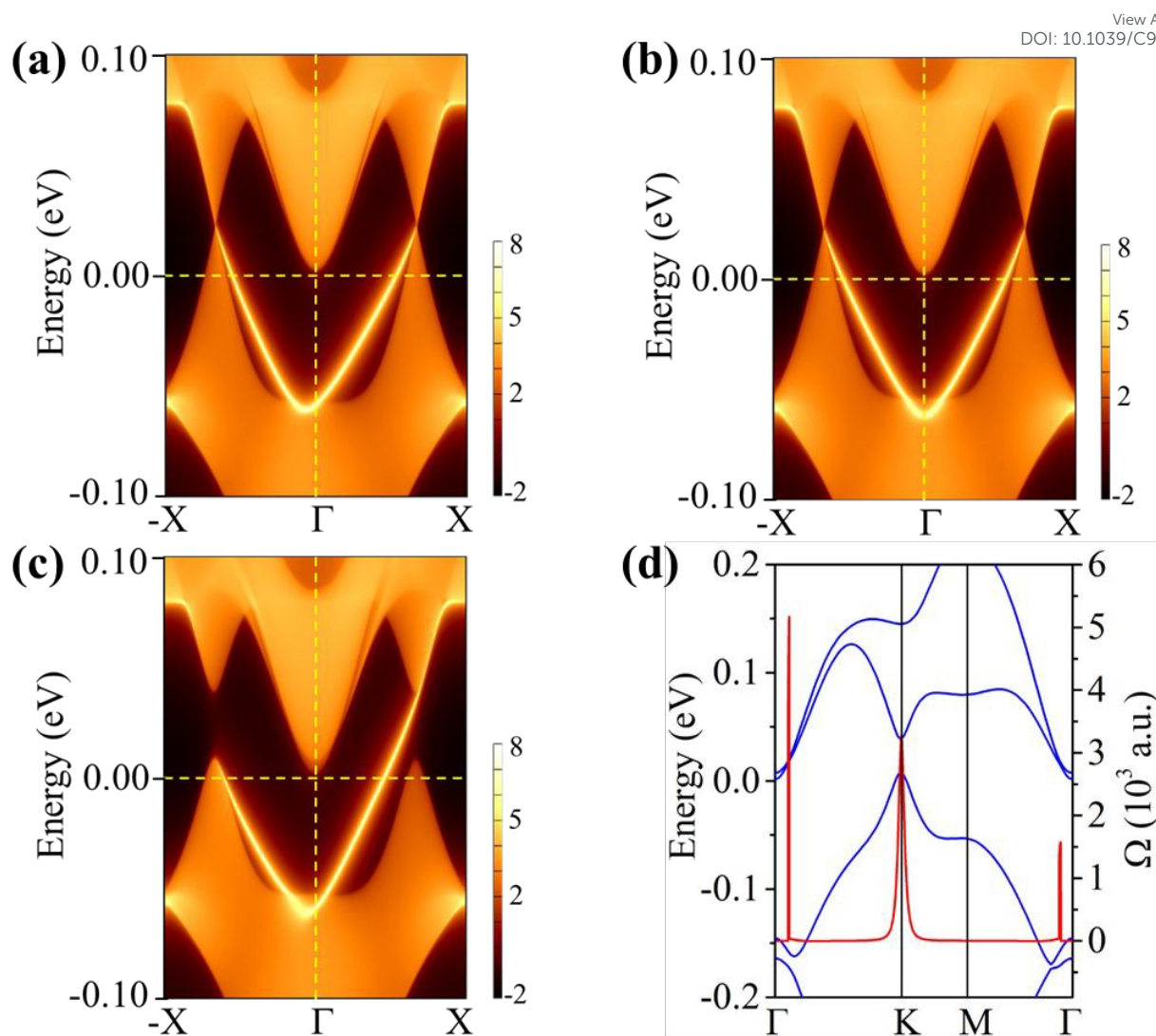


Figure 6. The edge states and the Berry curvature of monolayer VBr_3 . The V spins are in (a) FM^x , (b) FM^y and (c) FM^z configuration. (d) The distribution of the Berry curvature in momentum space for VBr_3 based on PBE method.

References

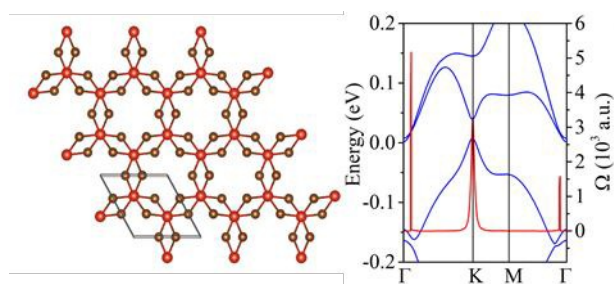
- 1 F. D. M. Haldane, Model for a Quantum Hall Effect without Landau Levels: Condensed-Matter Realization of the 'Parity Anomaly', *Phys. Rev. Lett.*, 1988, **61**, 2015–2018.
- 2 K. S. Novoselov, A. K. Geim, S. V. Morozov, D. Jiang, Y. Zhang, S. V. Dubonos, I. V. Grigorieva and A. A. Firsov, Electric Field Effect in Atomically Thin Carbon Films, *Science*, 2004, **306**, 666–669.
- 3 M. Ezawa, Spin valleytronics in silicene: Quantum spin Hall–quantum anomalous Hall insulators and single-valley semimetals, *Phys. Rev. B*, 2013, **87**, 155415.
- 4 G.-F. Zhang, Y. Li and C. Wu, Honeycomb lattice with multiorbital structure: Topological and quantum anomalous Hall insulators with large gaps, *Phys. Rev. B*, 2014, **90**, 075114.
- 5 S.-C. Wu, G. Shan and B. Yan, Prediction of Near-Room-Temperature Quantum Anomalous Hall Effect on Honeycomb Materials, *Phys. Rev. Lett.*, 2014, **113**, 256401.
- 6 S. Manzeli, D. Ovchinnikov, D. Pasquier, O. V. Yazyev and A. Kis, 2D transition metal dichalcogenides, *Nat. Rev. Mater.*, 2017, **2**, 17033.
- 7 C. Tan, X. Cao, X.-J. Wu, Q. He, J. Yang, X. Zhang, J. Chen, W. Zhao, S. Han, G.-H. Nam, M. Sindoro and H. Zhang, Recent Advances in Ultrathin Two-Dimensional Nanomaterials, *Chem. Rev.*, 2017, **117**, 6225–6331.
- 8 Y. Ren, Z. Qiao and Q. Niu, Topological Phases in Two-Dimensional Materials: A Brief Review, *Reports on Progress in Physics* 2016, **79**, 066501.
- 9 Z. Qiao, S. A. Yang, W. Feng, W.-K. Tse, J. Ding, Y. Yao, J. Wang and Q. Niu, Quantum anomalous Hall effect in graphene from Rashba and exchange effects, *Phys. Rev. B*, 2010, **82**, 161414.
- 10 Z. Qiao, W. Ren, H. Chen, L. Bellaiche, Z. Zhang, A. H. MacDonald and Q. Niu, Quantum Anomalous Hall Effect in Graphene Proximity Coupled to an Antiferromagnetic Insulator, *Phys. Rev. Lett.*, 2014, **112**, 116404.
- 11 J. Zhang, B. Zhao, Y. Yao and Z. Yang, Robust quantum anomalous Hall effect in graphene-based van der Waals heterostructures, *Phys. Rev. B - Condens. Matter Mater. Phys.*, 2015, **92**, 165418.
- 12 H. Zhang, C. Lazo, S. Blügel, S. Heinze and Y. Mokrousov, Electrically Tunable Quantum Anomalous Hall Effect in Graphene Decorated by 5d Transition-Metal Adatoms, *Phys. Rev. Lett.*, 2012, **108**, 056802.

- 13 J. Ding, Z. Qiao, W. Feng, Y. Yao and Q. Niu, Engineering quantum anomalous/valley Hall states in graphene via metal-atom adsorption: An ab-initio study, *Phys. Rev. B*, 2011, **84**, 195444.
- 14 R. Yu, W. Zhang, H.-J. Zhang, S.-C. Zhang, X. Dai and Z. Fang, Quantized Anomalous Hall Effect in Magnetic Topological Insulators, *Science*, 2010, **329**, 61–64.
- 15 J. G. Checkelsky, R. Yoshimi, A. Tsukazaki, K. S. Takahashi, Y. Kozuka, J. Falson, M. Kawasaki and Y. Tokura, Trajectory of the anomalous Hall effect towards the quantized state in a ferromagnetic topological insulator, *Nat. Phys.*, 2014, **10**, 731–736.
- 16 X. Kou, S. T. Guo, Y. Fan, L. Pan, M. Lang, Y. Jiang, Q. Shao, T. Nie, K. Murata, J. Tang, Y. Wang, L. He, T. K. Lee, W. L. Lee and K. L. Wang, Scale-invariant quantum anomalous hall effect in magnetic topological insulators beyond the two-dimensional limit, *Phys. Rev. Lett.*, 2014, **113**, 137201.
- 17 C.-Z. Chang, W. Zhao, D. Y. Kim, H. Zhang, B. A. Assaf, D. Heiman, S.-C. Zhang, C. Liu, M. H. W. Chan and J. S. Moodera, High-precision realization of robust quantum anomalous Hall state in a hard ferromagnetic topological insulator, *Nat. Mater.*, 2015, **14**, 473–477.
- 18 J. Wu, J. Liu and X. J. Liu, Topological spin texture in a quantum anomalous hall insulator, *Phys. Rev. Lett.*, 2014, **113**, 136403.
- 19 Q. L. He, L. Pan, A. L. Stern, E. C. Burks, X. Che, G. Yin, J. Wang, B. Lian, Q. Zhou, E. S. Choi, K. Murata, X. Kou, Z. Chen, T. Nie, Q. Shao, Y. Fan, S. C. Zhang, K. Liu, J. Xia and K. L. Wang, Chiral Majorana fermion modes in a quantum anomalous Hall insulator–superconductor structure, *Science*, 2017, **357**, 294–299.
- 20 P.-H. Chang, M. S. Bahramy, N. Nagaosa and B. K. Nikolić, Giant Thermoelectric Effect in Graphene-Based Topological Insulators with Heavy Adatoms and Nanopores, *Nano Lett.*, 2014, **14**, 3779–3784.
- 21 A. Cresti, D. Van Tuan, D. Soriano, A. W. Cummings and S. Roche, Multiple Quantum Phases in Graphene with Enhanced Spin-Orbit Coupling: From the Quantum Spin Hall Regime to the Spin Hall Effect and a Robust Metallic State, *Phys. Rev. Lett.*, 2014, **113**, 246603.
- 22 J. Zhang, B. Zhao, T. Zhou and Z. Yang, *Chinese Phys. B*, 2016, **25**, 117308.
- 23 G. Xu, B. Lian and S.-C. Zhang, Intrinsic Quantum Anomalous Hall Effect in the Kagome Lattice $\text{Cs}_2\text{LiMn}_3\text{F}_{12}$, 2015, **186802**, 1–5.
- 24 K. Dolui, S. Ray and T. Das, Intrinsic large gap quantum anomalous Hall

- insulators in LaX (X=Br, Cl, I), *Phys. Rev. B*, 2015, **92**, 205133.
- 25 J. He, X. Li, P. Lyu and P. Nachtigall, Near-room-temperature Chern insulator and Dirac spin-gapless semiconductor: nickel chloride monolayer, *Nanoscale*, 2017, **9**, 2246–2252.
- 26 X.-L. Sheng and B. K. Nikolić, Monolayer of the 5d transition metal trichloride OsCl_3 : A playground for two-dimensional magnetism, room-temperature quantum anomalous Hall effect, and topo, *Phys. Rev. B*, 2017, **95**, 201402.
- 27 C. Huang, J. Zhou, H. Wu, K. Deng, P. Jena and E. Kan, Quantum anomalous Hall effect in ferromagnetic transition metal halides, *Phys. Rev. B*, 2017, **95**, 045113.
- 28 B. Huang, G. Clark, E. Navarro-Moratalla, D. R. Klein, R. Cheng, K. L. Seyler, D. Zhong, E. Schmidgall, M. A. McGuire, D. H. Cobden, W. Yao, D. Xiao, P. Jarillo-Herrero and X. Xu, Layer-dependent ferromagnetism in a van der Waals crystal down to the monolayer limit, *Nature*, 2017, **546**, 270–273.
- 29 C. Gong, L. Li, Z. Li, H. Ji, A. Stern, Y. Xia, T. Cao, W. Bao, C. Wang, Y. Wang, Z. Q. Qiu, R. J. Cava, S. G. Louie, J. Xia and X. Zhang, Discovery of intrinsic ferromagnetism in two-dimensional van der Waals crystals, *Nature*, 2017, **546**, 265–269.
- 30 C. Huang, Y. Du, H. Wu, H. Xiang, K. Deng and E. Kan, Prediction of Intrinsic Ferromagnetic Ferroelectricity in a Transition-Metal Halide Monolayer, *Phys. Rev. Lett.*, 2018, **120**, 147601.
- 31 E. Torun, H. Sahin, S. K. Singh and F. M. Peeters, Stable half-metallic monolayers of FeCl_2 , *Appl. Phys. Lett.*, 2015, **106**, 192404.
- 32 S.-H. Zhang and B.-G. Liu, Intrinsic 2D ferromagnetism, quantum anomalous Hall conductivity, and fully-spin-polarized edge states of FeBr_3 monolayer, arXiv preprint arXiv:1706.08943 (2017).
- 33 W.-B. Zhang, Q. Qu, P. Zhu and C.-H. Lam, Robust Intrinsic Ferromagnetism and Half Semiconductivity in Stable Two-Dimensional Single-Layer Chromium Trihalides, 2015, **3**, 15–17.
- 34 C. Huang, J. Zhou, H. Wu, K. Deng, P. Jena and E. Kan, Quantum anomalous Hall effect in ferromagnetic transition metal halides, *Phys. Rev. B*, 2017, **95**, 045113.
- 35 Q. Sun and N. Kioussis, Intrinsic ferromagnetism and topological properties in two-dimensional rhenium halides, *Nanoscale*, 2019, **11**, 6101–6107.
- 36 Q. Sun and N. Kioussis, Prediction of manganese trihalides as two-dimensional Dirac half-metals, *Phys. Rev. B*, 2018, **97**, 094408.

- 37 J. Liu, Q. Sun, Y. Kawazoe and P. Jena, Exfoliating biocompatible ferromagnetic Cr-trihalide monolayers, *Phys. Chem. Chem. Phys.*, 2016, **18**, 8777–8784.
- 38 W.-B. Zhang, Q. Qu, P. Zhu and C.-H. Lam, Robust intrinsic ferromagnetism and half semiconductivity in stable two-dimensional single-layer chromium trihalides, *J. Mater. Chem. C*, 2015, **3**, 12457–12468.
- 39 N. Miao, B. Xu, L. Zhu, J. Zhou and Z. Sun, 2D Intrinsic Ferromagnets from van der Waals Antiferromagnets, *J. Am. Chem. Soc.*, 2018, **140**, 2417–2420.
- 40 W. Kohn and L. J. Sham, Self-Consistent Equations Including Exchange and Correlation Effects, *Phys. Rev.*, 1965, **140**, A1133–A1138.
- 41 G. Kresse, Ab initio molecular dynamics for liquid metals, *J. Non. Cryst. Solids*, 1995, **192–193**, 222–229.
- 42 P. E. Blöchl, Projector augmented-wave method, *Phys. Rev. B*, 1994, **50**, 17953–17979.
- 43 J. P. Perdew, K. Burke and M. Ernzerhof, Generalized Gradient Approximation Made Simple, *Phys. Rev. Lett.*, 1996, **77**, 3865–3868.
- 44 H. J. Monkhorst and J. D. Pack, Special points for Brillouin-zone integrations, *Phys. Rev. B*, 1976, **13**, 5188–5192.
- 45 S. L. Dudarev, G. A. Botton, S. Y. Savrasov, C. J. Humphreys and A. P. Sutton, Electron-energy-loss spectra and the structural stability of nickel oxide: An LSDA+U study, *Phys. Rev. B*, 1998, **57**, 1505–1509.
- 46 A. A. Mostofi, J. R. Yates, Y.-S. Lee, I. Souza, D. Vanderbilt and N. Marzari, wannier90: A tool for obtaining maximally-localised Wannier functions, *Comput. Phys. Commun.*, 2008, **178**, 685–699.
- 47 M. McGuire, Crystal and Magnetic Structures in Layered, Transition Metal Dihalides and Trihalides, *Crystals*, 2017, **7**, 121.
- 48 P. Liu, X. Luo, Y. Cheng, X.-W. Wang, W. Wang, H. Liu, K. Cho, W.-H. Wang and F. Lu, Physical realization of 2D spin liquid state by ab initio design and strain engineering in FeX₃, *J. Phys. Condens. Matter*, 2018, **30**, 325801.
- 49 Z. Li, B. Zhou and C. Luan, Strain-tunable magnetic anisotropy in two-dimensional Dirac half-metals: nickel trihalides, *RSC Adv.*, 2019, **9**, 35614–35623.
- 50 J.-Y. You, Z. Zhang, B. Gu and G. Su, Two-Dimensional Room-Temperature Ferromagnetic Semiconductors with Quantum Anomalous Hall Effect, *Phys. Rev. Appl.*, 2019, **12**, 024063.
- 51 Y. Wang, J. Lv, L. Zhu and Y. Ma, Crystal structure prediction via particle-

- swarm optimization, *Phys. Rev. B*, 2010, **82**, 094116.
- 52 Y. Wang, J. Lv, L. Zhu and Y. Ma, CALYPSO: A method for crystal structure prediction, *Comput. Phys. Commun.*, 2012, **183**, 2063–2070.
- 53 W. Wang, S. Dai, X. Li, J. Yang, D. J. Srolovitz and Q. Zheng, Measurement of the cleavage energy of graphite, *Nat. Commun.*, 2015, **6**, 7853.
- 54 P. W. Anderson, Antiferromagnetism. Theory of superexchange interaction, *Phys. Rev.*, , DOI:10.1103/PhysRev.79.350.
- 55 P. W. Anderson, Antiferromagnetism. Theory of Superexchange Interaction, *Phys. Rev.*, 1950, **79**, 350–356.
- 56 J. Kanamori, Superexchange interaction and symmetry properties of electron orbitals, *J. Phys. Chem. Solids*, 1959, **10**, 87–98.
- 57 J. Liu, Q. Sun, Y. Kawazoe and P. Jena, Exfoliating biocompatible ferromagnetic Cr-trihalide monolayers, *Phys. Chem. Chem. Phys.*, 2016, **18**, 8777–8784.
- 58 P. Li, Prediction of intrinsic two dimensional ferromagnetism realized quantum anomalous Hall effect, *Phys. Chem. Chem. Phys.*, 2019, **21**, 6712–6717.



View Article Online
DOI: 10.1039/C9CP05084A

It has been theoretically demonstrated that 2D transition metal trihalides can host the QAH effect.